

# SENSITIVE 21CM OBSERVATIONS OF NEUTRAL HYDROGEN IN THE LOCAL GROUP NEAR M31

SPENCER A. WOLFE

Dept. of Physics & Astronomy, West Virginia University, Morgantown, WV 26506

FELIX J. LOCKMAN

National Radio Astronomy Observatory <sup>1</sup>, Green Bank, WV 24944

D.J. PISANO

Dept. of Physics & Astronomy, West Virginia University, Morgantown, WV 26506

*Draft version March 2, 2024*

## ABSTRACT

Very sensitive 21cm HI measurements have been made at several locations around the Local Group galaxy M31 using the Green Bank Telescope (GBT) at an angular resolution of 9', with a  $5\sigma$  detection level of  $N_{\text{HI}} = 3.9 \times 10^{17} \text{ cm}^{-2}$  for a  $30 \text{ km s}^{-1}$  line. Most of the HI in a 12 square degree area almost equidistant between M31 and M33 is contained in nine discrete clouds that have a typical size of a few kpc and HI mass of  $10^5 M_{\odot}$ . Their velocities in the Local Group Standard of Rest lie between  $-100$  and  $+40 \text{ km s}^{-1}$ , comparable to the systemic velocities of M31 and M33. The clouds appear to be isolated kinematically and spatially from each other. The total HI mass of all nine clouds is  $1.4 \times 10^6 M_{\odot}$  for an adopted distance of 800 kpc with perhaps another  $0.2 \times 10^6 M_{\odot}$  in smaller clouds or more diffuse emission. The HI mass of each cloud is typically three orders of magnitude less than the dynamical (virial) mass needed to bind the cloud gravitationally. Although they have the size and HI mass of dwarf galaxies, the clouds are unlikely to be part of the satellite system of the Local Group as they lack stars. To the north of M31, sensitive HI measurements on a coarse grid find emission that may be associated with an extension of the M31 high-velocity cloud population to projected distances of  $\sim 100$  kpc. An extension of the M31 high-velocity cloud population at a similar distance to the south-east, toward M33, is not observed.

*Keywords:* galaxies: halos – galaxies: ISM – intergalactic medium – Local Group

## 1. INTRODUCTION

The two largest galaxies in the Local Group, M31 and the Milky Way, have a substantial amount of gas residing in a circumgalactic medium (CGM, also called a gaseous halo), outside of their disks. Their CGM is dominated by ionized gas, but also contains neutral high-velocity clouds (HVCs) observed in the 21cm line (Wakker 2001; Sembach et al. 2003; Thilker et al. 2004; Westmeier et al. 2008; Shull et al. 2009; Putman et al. 2009; Lehner et al. 2012, 2015). Gas likely associated with M31 is seen in absorption against background AGN to projected distances of at least 300 kpc (Lehner et al. 2015). The Milky Way may have a similar CGM less easily separated from disk gas because of projection effects, but manifest in the stripping of gas from dwarf spheroidals at distances to 300 kpc (Grcevich & Putman 2009; Spekkens et al. 2014; Gatto et al. 2013). If the CGM of M31 does extend this far, it encompasses the smaller spiral M33, which itself has a modest population of neutral HVCs (Grossi et al. 2008; Putman et al. 2009). The CGM of the Milky Way contains the Magellanic Stream (MS), which extends at least  $200^\circ$  across the sky in HI emission and whose mass is probably dominated by ionized

gas (Nidever et al. 2010; Fox et al. 2014).

There are also neutral atomic hydrogen (HI) clouds in the Local Group whose connection with individual galaxies is not understood. Compact high velocity clouds (CHVCs) and ultra-compact high velocity clouds (UCHVCs) are of small angular size and relatively isolated, and are candidates for low mass galaxies that may lack star formation entirely (de Heij et al. 2002; Adams et al. 2013). For a variety of reasons, CHVCs are now thought to reside in the Milky Way CGM (e.g., Sternberg et al. 2002), but the location and nature of the recently-discovered UCHVCs is less clear.

In their study of 21cm emission from HI in the Local Group, Braun & Thilker (2004, hereafter BT04), discovered extended regions of HI around the galaxy M31 that formed a partial bridge to the galaxy M33. This emission was detected at the extremely low levels of  $N_{\text{HI}} \sim 10^{17} \text{ cm}^{-2}$ , about two orders of magnitude below the typical column density detectable in extragalactic 21cm observations (Heald et al. 2011). The BT04 observations were made with a rather coarse angular resolution of  $49'$  and the origin of the neutral gas was uncertain, but the diffuse HI appeared to connect the systemic heliocentric velocities of M31 and M33 (Lewis et al. 2013). BT04 proposed that the HI arose from condensation in a dark matter-dominated filament connecting the two galaxies. Another suggestion was that it resulted from a tidal encounter between the galaxies (Bekki 2008). Subsequent observations of part of the region using the Green Bank

Electronic address: swolfe4@mix.wvu.edu  
 Electronic address: jlockman@nrao.edu  
 Electronic address: DJPisano@mail.wvu.edu

<sup>1</sup> The National Radio Astronomy Observatory is a facility of the National Science Foundation operated under a cooperative agreement by Associated Universities, Inc.

Telescope (GBT) at  $9'$  angular resolution confirmed the reality of the emission, though those data lacked the sensitivity to reveal any detailed structure (Lockman et al. 2012). As the existence and properties of CGM and intra-group gas is critical to our understanding of the formation and evolution of galaxies (e.g. Davé et al. 2001; Fukugita & Peebles 2006; Chen et al. 2010; Putman et al. 2012; Cen 2013; Lehner et al. 2015), we have undertaken a major survey of the area around and between M31 and M33 using the Green Bank Telescope, which provides both the sensitivity needed to detect this extremely faint emission, and the angular resolution to discern some of its structure.

In a previous paper (Wolfe et al. 2013, hereafter Paper I) we presented results of the first part of the study, which showed that a significant fraction of the HI detected in a 12 square-degree field south-east of M31 in the direction of M33 arose in discrete structures which, assuming they are 800 kpc distant, have the size of dwarf galaxies but no detectable stellar component. Subsequently, Martin et al. (2013) suggested that there may be a stellar overdensity in the direction of one of the clouds, but the association between the gas and stars is not established at this time. The clouds have velocities similar to the systemic velocities of M31 and M33 and are thus probably not part of the high-velocity cloud (HVC) system of either galaxy. Here we report on additional observations that reveal more clearly the structure and content of the HI clouds, as well as new observations of selected directions to the north of M31. The distances to M31 and M33 are  $\sim 750$  and  $\sim 850$  kpc, respectively (e.g. Riess et al. 2012; Bono et al. 2010) so we assume that the material located between them lies at a distance of 800 kpc.

## 2. OBSERVATIONS

All data used here were obtained with the 100-meter Robert C. Byrd Green Bank Telescope (GBT, Prestage et al. 2009) with the dual-polarization L-band receiver that has a total system temperature of  $\lesssim 18$  K at elevations  $> 20^\circ$ . At the frequency of the 21cm line, the telescope has a half-power beam-width of  $9'.1$ . Spectra were measured using the GBT Spectrometer, which provides a total velocity coverage  $> 1000$  km s $^{-1}$  in the 21cm line at a channel spacing of 0.32 km s $^{-1}$ . Spectra were calibrated using observations of 3C48 and the antenna response analysis from Boothroyd et al. (2011). Velocities were measured with respect to the Local Standard of Rest (LSR), but in this part of the sky,  $V_{\text{LSR}}$  differs from heliocentric velocities by only a few km s $^{-1}$ .

Figure 1 shows the observed areas on the BT04 HI map of the region. Data reduction was done with special procedures written in GBTIDL (Marganian et al. 2006), the stray radiation correction and calibration followed Boothroyd et al. (2011), and special procedures were written to remove instrumental baselines from spectra in the data cube.

### 2.1. The M31-M33 Field

As described in Paper I, we used the GBT to map a  $6^\circ \times 2^\circ$  field in right ascension and declination centered at J2000 =  $01^{\text{h}}16^{\text{m}} + 37^\circ00'$ . The observations were made while moving the telescope in right ascension at a fixed declination, binning the data in 3-second samples every

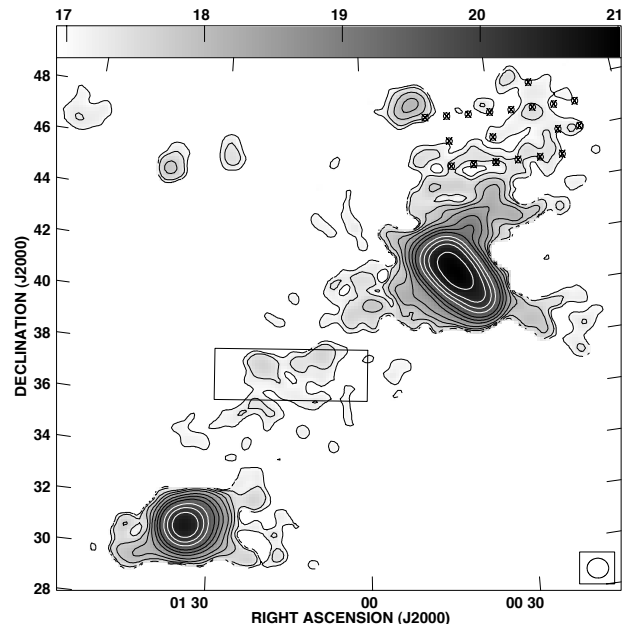


**Figure 1.** Locations of the current observations marked on a map of the total  $N_{\text{HI}}$  from the BT04 survey. The galaxies M33 and M31 lie at the lower left and upper right, respectively. Contours are for  $\log(N_{\text{HI}}) = 17.0, 17.3, 17.7, 18.0, 18.3, 18.7, 19.0, 19.3, 19.7, 20.0, 20.3$  and  $20.7$  ( $\text{cm}^{-2}$ ). Our “M31-M33” field, outlined with a box, lies between the two galaxies and was covered with complete sampling. North of M31, we made a series of pointed observations at locations marked with boxed crosses. The GBT angular resolution is  $9'$ , but the boxed crosses are  $15'$  in size to make them easier to see. The boxed circle in the lower right shows the resolution of BT04.

$1'.6$  in right ascension. At the end of the  $6^\circ$  strip the telescope was stepped in declination by  $3'.6$  and the scanning direction was reversed. This procedure covered the area with Nyquist sampling in declination, and finer sampling in the moving coordinate to prevent beam broadening (Mangum et al. 2007). Regions at eastern edge of each row – areas identified as having no emission by BT04 and confirmed from our observations – were used as reference positions. Spectra from the eastern-most  $16'$  of each strip were averaged and supplied the reference spectrum for the rest of the spectra in the strip. As the reference spectrum had an integration time of 30 seconds, this greatly reduced the noise in the difference spectrum. The field was observed over and over again until the desired noise level was reached. In all, the M31-M33 field was observed for about 400 hours with an average time per GBT beam of 46 min. Our observing procedure could cancel some emission, but only if it had a nearly constant amplitude and  $V_{\text{LSR}}$  over scales of many degrees. We see no evidence of this in the data. There are three positions in our map where Lockman et al. (2012) made frequency-switched detections of HI emission associated with the clouds. Those data are in reasonable agreement with our current measurements. At another position where only a small upper limit was reported, we likewise see no emission. This indicates that our position-switched technique has not cancelled significant amounts of HI. In addition, the current data are consistent with the sensitive GBT spectrum reported in BT04, but note that the declination reported in BT04 has a typograph-

ical error: the correct position of the GBT spectrum is  $J2000 = 01^{\text{h}}20^{\text{m}}29'' + 37^{\circ}22'33''$ .

Spectra were corrected for atmospheric attenuation and a second-order polynomial was fit to emission-free channels to provide statistics for a quick check on data quality. In general, instrumental baselines were excellent and modeled well by a 2nd or 3rd order polynomial. A small fraction of the spectra (4%) was rejected for having poor instrumental baselines caused mainly by radio frequency interference or temporary instrumental effects. The spectra were smoothed to an effective velocity resolution of  $5.15 \text{ km s}^{-1}$  and gridded into a cube using *AIPS*<sup>2</sup> with a pixel spacing of  $1.75$  using a spherical Bessel interpolation function following Mangum et al. (2007). A third-order baseline was removed from each spectrum in the cube. The procedure of subtracting a nearby reference position should effectively remove stray radiation (Boothroyd et al. 2011) hence no further corrections were applied. The noise in the final cube varies slightly with position, with a typical value, in brightness temperature, of  $\sigma_T = 3.45 \text{ mK}$  in a  $5.15 \text{ km s}^{-1}$  channel. This gives a  $5\sigma$  limit on  $N_{\text{HI}}$  of  $3.9 \times 10^{17}$  for a  $30 \text{ km s}^{-1}$  FWHM line. The equivalent H I mass limit is  $\sim 10^4 M_{\odot}$ , assuming a distance of  $800 \text{ kpc}$ . We note that previous surveys around galaxy groups typically have mass limits  $\gtrsim 10^5 M_{\odot}$  (Auld et al. 2006) or  $10^6 M_{\odot}$  (e.g. Zwaan 2001; Pisano et al. 2007; Chynoweth et al. 2008).

## 2.2. M31 North Observations

Observations were also made at 18 positions north of M31 to investigate the nature of the very faint 21cm emission detected by BT04 in this area. The observed positions are shown in Figure 1. Here, because reference positions were not readily available, the data were taken by frequency switching between the 21cm rest frequency and a band  $4 \text{ MHz}$  ( $844 \text{ km s}^{-1}$ ) away within the  $12.5 \text{ MHz}$  band of the GBT Spectrometer. Data were calibrated and corrected for stray radiation as described by Boothroyd et al. (2011), and a third or fourth order polynomial was fit to emission-free velocities. The data were then smoothed from  $0.3 \text{ km s}^{-1}$  velocity resolution to  $1.3 \text{ km s}^{-1}$ . The typical on-source integration time for each pointing is 76 minutes and the median noise in a  $1.3 \text{ km s}^{-1}$  channel is  $3.7 \text{ mK}$ . This gives a  $5\sigma$  limit on  $N_{\text{HI}}$  of  $1.6 \times 10^{17} \text{ cm}^{-2}$  for a spectral line with a full width at half maximum (FWHM) of  $30 \text{ km s}^{-1}$ .

## 3. NEUTRAL HYDROGEN BETWEEN M31 AND M33

An integrated intensity map of the spectra summed over  $-359 \leq V_{\text{LSR}} \leq -187 \text{ km s}^{-1}$  and converted to column density,  $N_{\text{HI}}$ , is presented in Figure 2. This range encompasses all detected HI emission not associated with the Milky Way. Emission from the disks of M31 and M33 overlaps that from the Milky Way at some  $V_{\text{LSR}} \geq -150 \text{ km s}^{-1}$ , but these velocities are not in the range studied here.  $N_{\text{HI}}$  is calculated under the assumption that the emission is optically thin, an excellent assumption for lines with  $T_b < 100 \text{ mK}$ . The rms noise in column density is  $1.9 \times 10^{17} \text{ cm}^{-2}$  ( $1\sigma$ ); contours are drawn in multiples of  $5 \times 10^{17} \text{ cm}^{-2}$ . The HI emission in this field is dominated by discrete clouds, some of which

are resolved by the GBT  $9.1$  beam. Six of these clouds were detected at full angular resolution in Paper I, the other three appear in the more sensitive data presented here. Spectra toward the peak  $N_{\text{HI}}$  of each cloud are shown in Figure 3.

A Gaussian function was fit to the 21cm spectrum of each cloud at the location of its peak  $N_{\text{HI}}$ , and the components, along with the location of the peak, are given in Table 1. Errors are  $1\sigma$  from the Gaussian fit. Clouds are numbered for convenience; the identification is usually not the same as in Paper I.

Table 2 gives derived properties of the clouds. The velocity with respect to the Local Group ( $V_{\text{LSR}}$ ) was determined using the calculator given in NED<sup>3</sup>. The quantity *Diam* is the maximum cloud extent measured down to the  $3\sigma$  noise level while  $\langle \text{Diam} \rangle$  is the diameter of a circle with an area equal to that of the cloud. The difference between these quantities is a measure of the elongation of a cloud. The “average FWHM” of the 21cm line averaged over the entire cloud is given in Col. 5. Cloud 8 was not completely mapped so some of its quantities are limits. There is an additional emission feature at the very north-west edge of the field,  $J2000 = 01^{\text{h}}00^{\text{m}}24^{\text{s}} + 37^{\circ}53'$  with  $T_b \approx 10 \text{ mK}$  at  $V_{\text{LSR}} = -264 \text{ km s}^{-1}$  and a peak  $N_{\text{HI}} \lesssim 10^{18} \text{ cm}^{-2}$ , but we cannot characterize it further.

The HI mass in Col. 7 was calculated by integrating over velocities relevant to each cloud, then summing over an area around the cloud. The mass assumes that the emission is optically thin. Errors on the mass are derived from the noise in emission-free channels over the area of each cloud.

A two-dimensional Gaussian was fit to each cloud yielding a major and minor axis size. For this, the two parts of Cloud 3 were treated separately. Major and minor axis radii from the Gaussian fitting were then deconvolved to produce an estimate of the true angular size given the  $9.1$  beam of the GBT, which is approximately Gaussian:  $r_{\text{true}} = (r_{\text{obs}}^2 - 4.55^2)^{1/2}$ . The minor axis of Clouds 1, 3b and 4 were unresolved within the errors, and for these we assume an intrinsic radius of  $1'$ , equivalent to  $233 \text{ pc}$  at the assumed  $800 \text{ kpc}$  distance of the clouds. Quantities derived from this adopted radius are consequently uncertain, and are marked with a colon (:) in Table 2. The square root of the product of the deconvolved major and minor axis radii is given in Col. 6 of Table 2 and called  $r_{1/2}$ . This is the average radius within which half the HI mass is contained as estimated from the deconvolved Gaussian fit.

Using this radius we calculate a dynamical (or virial) mass – the total mass (from whatever source) needed to bind a cloud of radius  $r_{1/2}$  that has a given velocity dispersion. We note that the definition of the *dynamical* or *virial* or *total* mass derived from the size and velocity structure of an object differs considerably from author to author, and an exact determination requires information that we do not possess, such as the density structure within a cloud. For simplicity, and to allow comparisons with other measurements (see §6) we adopt the following

<sup>2</sup> Developed by the National Radio Astronomy Observatory: <http://www.aips.nrao.edu/index.shtml>.

<sup>3</sup> The NASA/IPAC Extragalactic Database is operated by the Jet Propulsion Laboratory, California Institute of Technology, under contract with the National Aeronautics and Space Administration.

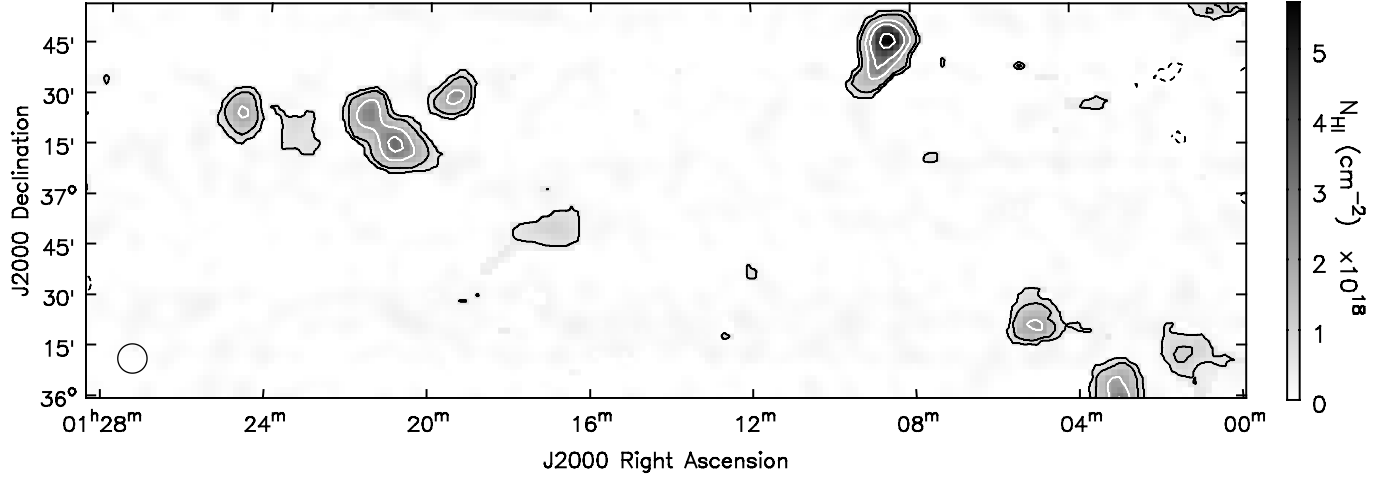


**Figure 2.** Integrated HI column density map of the M31-M33 clouds over  $-359 \leq V_{\text{LSR}} \leq -187 \text{ km s}^{-1}$ . The contours are at -1, 1, 2, 4, 6 and 10 times increments of  $5 \times 10^{17} \text{ cm}^{-2}$ . The circle in the lower left shows the angular resolution of the GBT.

**Table 1**  
Clouds Detected Between M31 and M33

Cloud (1)	J2000 (hh:mm:ss dd:mm:ss) (2)	$T_L$ (mK) (3)	FWHM ( $\text{km s}^{-1}$ ) (4)	$V_{\text{LSR}}$ ( $\text{km s}^{-1}$ ) (5)	$N_{\text{HI}}$ ( $10^{18} \text{ cm}^{-2}$ ) (6)
1	01:24:41.6 +37:24:00	$44.0 \pm 2.4$	$25.5 \pm 1.6$	$-297.8 \pm 0.7$	$2.2 \pm 0.1$
2	01:23:21.7 +37:18:45	$10.9 \pm 2.2$	$39.3 \pm 9.3$	$-223.0 \pm 4.0$	$0.8 \pm 0.1$
3	01:20:51.8 +37:15:15	$63.2 \pm 1.8$	$27.2 \pm 0.9$	$-237.3 \pm 0.4$	$3.3 \pm 0.1$
4	01:19:15.8 +37:29:15	$28.5 \pm 2.1$	$38.1 \pm 3.3$	$-228.2 \pm 1.4$	$2.2 \pm 0.1$
5	01:16:53.7 +36:49:00	$18.3 \pm 1.7$	$26.2 \pm 3.0$	$-308.7 \pm 1.2$	$0.9 \pm 0.1$
6	01:08:29.6 +37:45:00	$81.3 \pm 3.6$	$32.0 \pm 1.9$	$-278.6 \pm 0.6$	$5.0 \pm 0.1$
7	01:05:00.3 +36:21:00	$34.7 \pm 3.0$	$31.4 \pm 3.5$	$-210.2 \pm 1.2$	$2.1 \pm 0.2$
8	01:03:01.8 +36:00:00	$35.0 \pm 2.6$	$36.8 \pm 3.4$	$-281.4 \pm 1.3$	$2.5 \pm 0.2$
9	01:01:24.6 +36:12:15	$25.4 \pm 3.2$	$19.2 \pm 2.9$	$-341.0 \pm 1.2$	$0.9 \pm 0.1$

**Table 2**  
Derived Cloud Properties<sup>a</sup>

Cloud (1)	$V_{\text{LSR}}$ ( $\text{km s}^{-1}$ ) (2)	Diam <sup>b</sup> (kpc) (3)	$\langle \text{Diam} \rangle^c$ (kpc) (4)	$\langle \text{FWHM} \rangle^d$ ( $\text{km s}^{-1}$ ) (5)	$r_{1/2}^e$ (kpc) (6)	$M_{\text{HI}}$ ( $10^4 M_\odot$ ) (7)	$M_{\text{dyn}}^f$ ( $10^8 M_\odot$ ) (8)	$\rho^g$ (kpc) (9)
1	-61	4.4	3.2	$22.2 \pm 0.6$	0.38:	$12.7 \pm 0.2$	0.5:	126
2	+14	4.4	2.8	$28.0 \pm 3.5$	0.75	$4.5 \pm 0.2$	1.5	123
3	+1	7.2	5.3	$27.6 \pm 0.8$		$33.0 \pm 0.3$		118
3a				$28.0 \pm 1.0$	0.82	$22.7 \pm 0.2$	1.6	
3b				$27.1 \pm 1.3$	0.34:	$10.2 \pm 0.2$	0.6:	
4	+12	3.7	3.1	$26.5 \pm 1.5$	0.41:	$8.6 \pm 0.2$	0.7:	112
5	-69	7.0	3.8	$21.8 \pm 2.5$	1.13	$7.8 \pm 0.2$	1.3	109
6	-32	7.2	4.6	$33.6 \pm 1.3$	0.78	$39.2 \pm 0.3$	2.2	87
7	+36	4.9	3.9	$27.4 \pm 2.1$	0.71	$12.6 \pm 0.4$	1.3	92
8	-35	> 3.5	> 3.2	$29.6 \pm 2.1$		> 11.6		91
9	-94	3.5	3.2	$20.5 \pm 2.3$	0.96	$8.7 \pm 0.2$	1.0	88

<sup>a</sup> For an assumed distance of 800 kpc.

<sup>b</sup> Maximum cloud extent.

<sup>c</sup> Diameter of a circle with an area equal to that of the cloud.

<sup>d</sup> Column density weighted average FWHM over the entire cloud.

<sup>e</sup> Square root of the product of the major and minor axis radii.

<sup>f</sup> From Equation 2.

<sup>g</sup> Projected distance from M31.

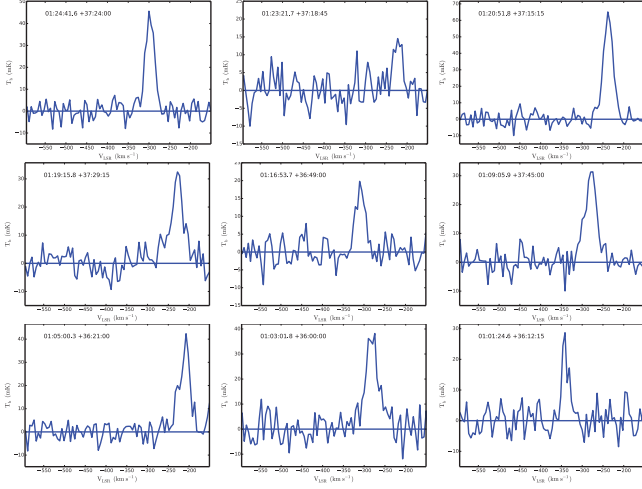


**Figure 3.** Spectra taken at the peak  $N_{\text{HI}}$  of the nine clouds detected in the M31-M33 field. The vertical axis is 21cm brightness temperature and the horizontal axis is  $V_{\text{LSR}}$ .

(Binney & Tremaine 2008):

$$M_{\text{dyn}} \equiv \frac{2 r_{1/2} \sigma_v^2}{G}, \quad (1)$$

where  $G$  is the gravitational constant and  $\sigma_v$  is the 3-dimensional velocity dispersion of the cloud. As  $\sigma_v$  is not a measurable quantity, we use the FWHM from the measured average spectrum, and assume isotropy to calculate

$$\left( \frac{M_{\text{dyn}}}{M_{\odot}} \right) \equiv 2.5 \times 10^5 \left( \frac{r_{1/2}}{\text{kpc}} \right) \left( \frac{\text{FWHM}}{\text{km s}^{-1}} \right)^2, \quad (2)$$

where  $r_{1/2}$  is in kpc, FWHM in  $\text{km s}^{-1}$  and  $M_{\text{dyn}}$  is in solar masses. Dynamical masses are given in Col. 8. In all cases they exceed the observed HI mass by a factor of  $\sim 10^3$ . Col. 9 gives  $\rho$ , the projected distance from M31 assuming that the clouds are at a distance of 800 kpc. The clouds lie  $\gtrsim 90$  kpc away from M31's center, farther than the distances of the known HVCs around M31, all of which have  $\rho < 50$  kpc (Westmeier et al. 2008).

### 3.1. The Velocity Range

In the field of Figure 2, we find no HI emission at velocities more negative than that associated with cloud 9, i.e., nothing at  $V_{\text{LSR}} \lesssim -370 \text{ km s}^{-1}$  and no emission at the more positive velocities between  $-190 \lesssim V_{\text{LSR}} \lesssim -160 \text{ km s}^{-1}$ . At still more positive  $V_{\text{LSR}}$ , there is a band of HI extending from the south center of the field to the north-west that is quite bright by our standards ( $T_b > 0.6 \text{ K}$ ) at  $-150 \lesssim V_{\text{LSR}} \lesssim -100 \text{ km s}^{-1}$ . This appears to connect smoothly to Milky Way emission at more positive velocity and we will not consider it further here.

Lehner et al. (2015) argue that the CGM of M31 should be defined as having  $-300 \lesssim V_{\text{LSR}} \lesssim -150 \text{ km s}^{-1}$ , that velocities more negative than this may arise in the Magellanic Stream and velocities more positive in the halo of the Milky Way. Our Cloud 9 has a peak  $N_{\text{HI}}$  at  $V_{\text{LSR}} = -341 \text{ km s}^{-1}$ , but is in no way unusual in its size, mass, linewidth, or projected distance from M31, so we assume that it is part of the cloud population. Westmeier et al. (2008) have detected 21cm emission that

they attribute to M31 HVCs only  $\sim 2^\circ$  to the northwest of the Figure 2 field at velocities as negative as  $V_{\text{LSR}} \approx -500 \text{ km s}^{-1}$ . We would have easily detected similar emission in the Figure 2 field. Apparently the M31 HVC population does not extend over this area. This will be discussed further in §6.

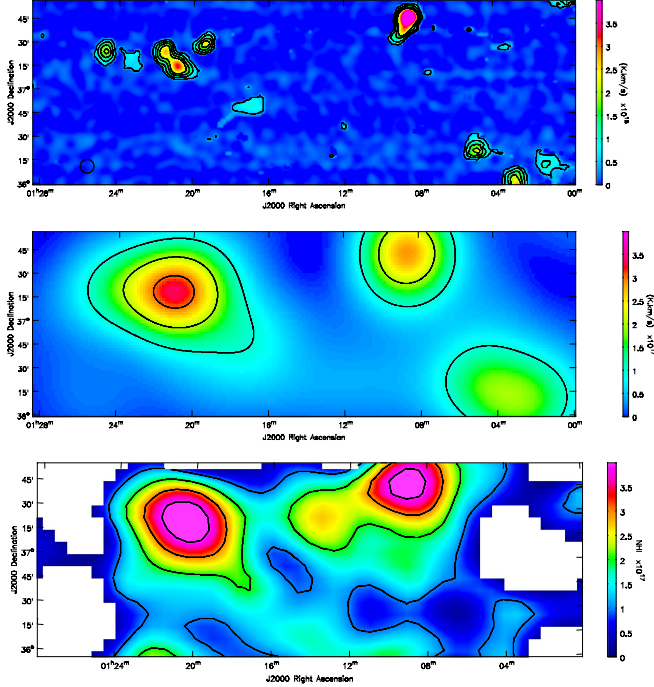
### 3.2. The Total Neutral Hydrogen Mass

Figure 2 shows some evidence for HI emission outside of the clouds listed in Table 1, but this is relatively small and usually concentrated in discrete regions. Assuming that all the HI we detect is at a distance of 800 kpc, the sum of the HI mass of all nine clouds is  $1.4 \times 10^6 M_{\odot}$ , while integration over the entire field yields  $1.6 \times 10^6 M_{\odot}$ . Thus virtually all of the neutral gas we measure is contained in the nine clouds with about half in just the two largest clouds, numbers 3 and 6.

To compare our data with those of BT04, we match the angular resolution of that survey by convolving the integrated spectra shown in Figure 2 to an angular resolution of  $49'$  using the WSRT beam from Popping & Braun (2008). Results are shown in Figure 4. While the maps have many similarities there are significant differences. The most striking is near J2000 =  $01^h 13^m 30^s, +37^\circ 24'$ , where the BT04 data show emission that does not appear in the GBT data. The BT04 survey also contains emission at the south-central part of our field, some of which may arise from a cloud just off our map at  $01^h 10^m, +35^\circ 30'$  convolved with the much larger BT04 beam. In some areas we find good agreement between the two surveys – the northwest and northeast corners, for example – but overall BT04 reports an HI mass  $2.5 \times 10^6 M_{\odot}$  for the area, while we find only 63% of this amount.

We believe that the cause of this discrepancy lies mostly, though not entirely, in the choice of velocity range of integration for the BT04 survey. No emission is detected with the GBT at velocities more negative than  $-370 \text{ km s}^{-1}$ . If the GBT data are integrated over all velocities  $\leq -150 \text{ km s}^{-1}$ , the total mass remains  $1.6 \times 10^6 M_{\odot}$ , but if the upper limit is taken to be  $-140 \text{ km s}^{-1}$ , only  $10 \text{ km s}^{-1}$  more positive, the total HI mass doubles. We discuss above the reasons for not including emission at  $V_{\text{LSR}} \geq -150 \text{ km s}^{-1}$  in the census of Local Group gas, as it likely arises in the Milky Way (Lehner et al. (2015) conclude this as well). It is plausible that some of this emission is present in the BT04 map, especially as those spectra had a rather coarse velocity resolution of  $17 \text{ km s}^{-1}$ . This explanation does not account for the discrepancy with the BT04 feature at  $01^h 13^m 30^s + 37^\circ 24'$ . The GBT spectrum in this direction is entirely consistent with noise at  $V_{\text{LSR}} \leq -145 \text{ km s}^{-1}$ .

In Paper I we reported that there was  $\approx 1 \times 10^6 M_{\odot}$  of HI in the GBT data that was not associated with discrete clouds. We now believe that this conclusion is incorrect and resulted from a very small systematic baseline error with an amplitude of only a few mK in the preliminary GBT data. In the current data there can be no more than  $0.2 \times 10^6 M_{\odot}$  of HI outside the nine clouds. We do not believe that our data reduction procedure is artificially suppressing real emission; instrumental baseline fitting removes only low-order polynomials preserving lines of normal velocity width, and the position-switching observing technique preserves structure on an



**Figure 4.** Top panel: integral column density of the M31-M33 field at full GBT angular resolution; contours are every  $5 \times 10^{17} \text{ cm}^{-2}$  beginning at  $5 \times 10^{17} \text{ cm}^{-2}$  and the color scale runs from zero to  $4 \times 10^{18} \text{ cm}^{-2}$ . Middle panel: GBT data smoothed to the  $49'$  angular resolution of the BT04 measurements using the WSRT beam from Popping & Braun (2008). For this and the lower panel, the color scale runs from zero to  $4 \times 10^{17} \text{ cm}^{-2}$ , and the contours are every  $10^{17} \text{ cm}^{-2}$  beginning at  $10^{17} \text{ cm}^{-2}$ . Lower panel: BT04 integral column density map at  $49'$  resolution. Regions without detectable HI are blanked. While many of the general features of our GBT data agree with those from BT04, the BT04 map contains regions of emission not found in the GBT data.

gular scales  $\lesssim 5^\circ$ . If there were emission in the reference regions beyond the edge of the map, we would see it as negative features in the map. As no such features exist, we have confidence in our estimates of  $M_{\text{HI}}$ .

### 3.3. Velocity and Linewidth

The average velocity of the HI emission is shown pixel-by-pixel in Figure 5. Contours are the same as in Figure 2. Here, to give an indication of the overall velocity pattern of the clouds the velocity-weighted values of the brightness temperature were calculated over the entire range of detectable emission:  $-359$  to  $-187 \text{ km s}^{-1}$ , clipping the data at the approximate  $4\sigma$  noise level of 15 mK. The clouds span a range of velocity between  $-341 \leq V_{\text{LSR}} \leq -210 \text{ km s}^{-1}$ . In our data, there are only two clouds that have significant internal velocity structure. These are shown in Figures 6 and 7.

Cloud 3 consists of two components with nearly identical velocities at their peak, but overall there is a  $10 \text{ km s}^{-1}$  gradient from  $-240 \text{ km s}^{-1}$  between the two cloud components to  $-233 \text{ km s}^{-1}$  at the northern edge and  $-230 \text{ km s}^{-1}$  at the southern edge. Cloud 6 has a head-tail appearance with, once again, velocities most negative at the center and rising by  $\approx 10 \text{ km s}^{-1}$  at the northern and southern edges.

The mean linewidth at the peak  $N_{\text{HI}}$  of the nine clouds is  $27.9 \pm 4.3 \text{ km s}^{-1}$ , essentially identical to the median. The lines are well-fit by single Gaussians. Unlike Galactic HVCs and CHVCS, there is no evidence for two

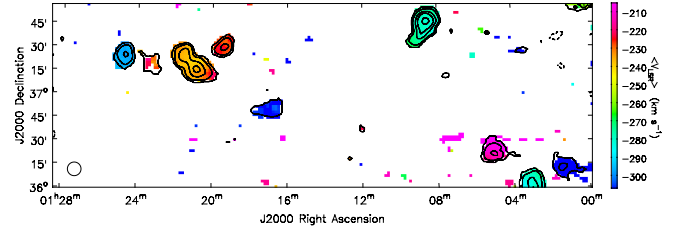


**Figure 5.** Average  $V_{\text{LSR}}$  over the field, calculated for channels between  $-359 \leq V_{\text{LSR}} \leq -187 \text{ km s}^{-1}$  that have  $T_b > 4\sigma = 0.015 \text{ K}$ . Although velocities can vary significantly from cloud to cloud, the mean velocity within a cloud is relatively constant. The circle in the lower left shows the angular resolution of the GBT. It is apparent that the clouds are separated not only spatially but kinematically.

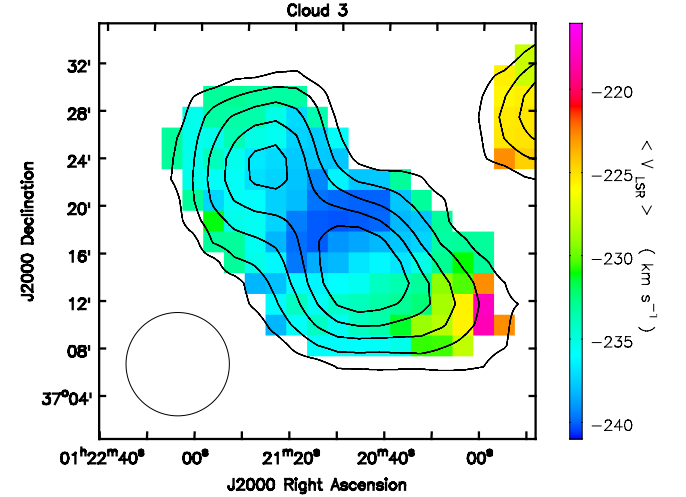


**Figure 6.** Average  $V_{\text{LSR}}$  pixel-by-pixel for Cloud 3 together with contours of  $N_{\text{HI}}$ . Averages were calculated only for channels with  $T_b > 4\sigma = 15 \text{ mK}$ . Contours are at 1, 2, 3, 4, and 5 times increments of  $5 \times 10^{17} \text{ cm}^{-2}$ . Unrelated emission from Cloud 4 appears in the upper right. The circle in the lower left shows the angular resolution of the GBT. Both cloud components show a  $10 \text{ km s}^{-1}$  velocity gradient between their center and edge.

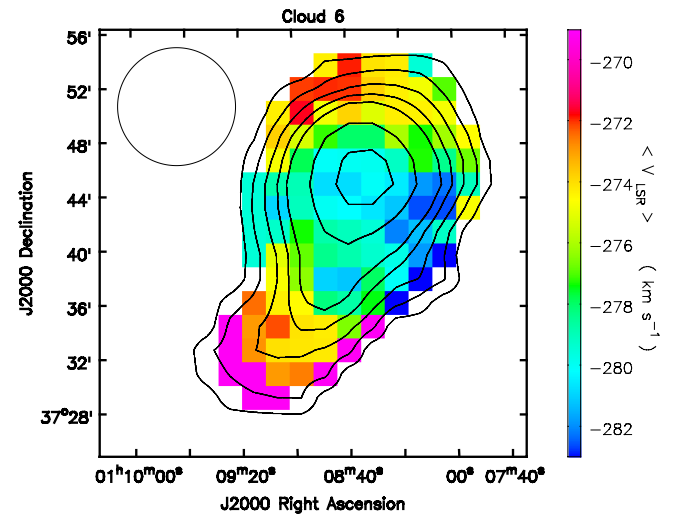


**Figure 7.** Average  $V_{\text{LSR}}$  pixel-by-pixel for Cloud 6 together with contours of  $N_{\text{HI}}$ . Averages were calculated only for channels with  $T_b > 4\sigma = 15 \text{ mK}$ . Contours are at 1, 2, 3, 4, 5, 7.5 and 10 times increments of  $5 \times 10^{17} \text{ cm}^{-2}$ . The circle in the upper left shows the angular resolution of the GBT. This cloud shows a  $10 \text{ km s}^{-1}$  velocity gradient from the center to its edges.



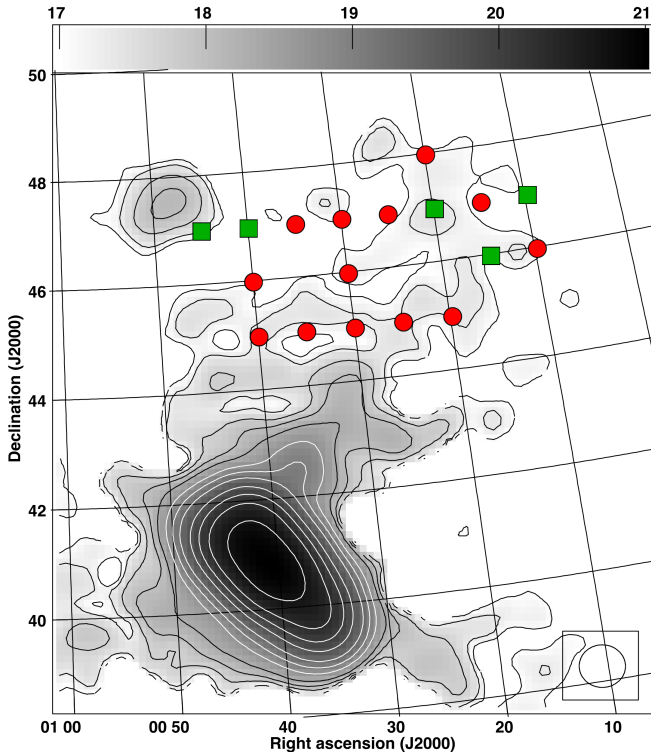


**Figure 8.** Expanded view of the BT04 survey HI data from Figure 1 to show the locations of the GBT measurements to the northwest of M31. The GBT angular resolution is  $9'$ , but the symbols are  $15'$  across for easier identification. Green boxes mark positions with detected HI emission at  $V_{\text{LSR}} \leq -150 \text{ km s}^{-1}$ . Red circles show positions without a detection. The circle in the lower right shows the BT04 angular resolution.

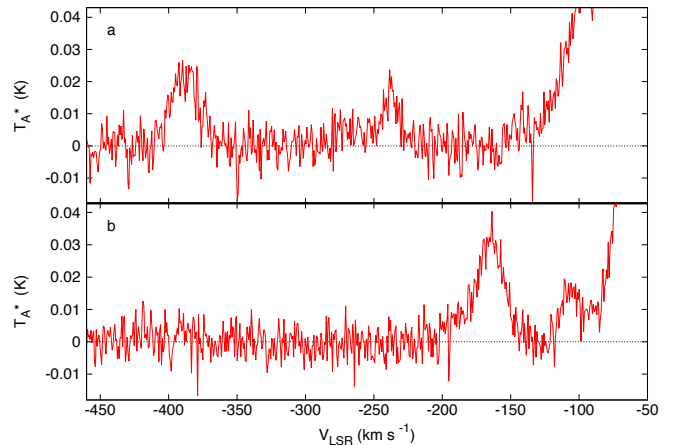
components in any of the lines as would be expected if they have a two-phase temperature structure (Sternberg et al. 2002). The FWHM does not vary much across an individual cloud. The FWHM averaged over the entire cloud (Table 2) and toward the peak  $N_{\text{HI}}$  (Table 1) are quite similar. The range of linewidths is  $19.2 - 32.5 \text{ km s}^{-1}$ , much smaller than the range observed in 17 M31 HVCs (at essentially identical angular resolution) of  $11 - 71 \text{ km s}^{-1}$  (Westmeier et al. 2008).

Figure 5 re-enforces the impression from Figure 2 that the individual clouds are independent entities, as nearby clouds can have quite different velocities. Clouds 7 and 9, for example, differ by  $120 \text{ km s}^{-1}$  yet are separated by  $< 1^\circ$  on the sky ( $\sim 10 \text{ kpc}$  at  $800 \text{ kpc}$  distance).

#### 4. NEUTRAL HYDROGEN TO THE NORTH OF M31

Results from the measurements to the north of M31 are given in Table 3, and illustrated in Figure 8 as symbols on a map of the BT04 survey. We include only emission with  $V_{\text{LSR}} \leq -150 \text{ km s}^{-1}$ . Line properties were derived from a Gaussian fit, and errors are  $1\sigma$ . Values of  $N_{\text{HI}}$  come also from the Gaussian fit; here errors reflect both the noise and an assumed equal contribution from baseline uncertainties. The median  $5\sigma$  sensitivity to a  $30 \text{ km s}^{-1}$  FWHM line is  $1.6 \times 10^{17} \text{ cm}^{-2}$ . Because we have only incomplete sampling, it is not possible to delineate objects and calculate a mass or size. The values of  $N_{\text{HI}}$  should be understood as random samples of the medium and not peak values, in contrast to the values given in Table 1 for the M31-M33 field.

Our results are rather puzzling in view of the BT04



**Figure 9.** [a] Spectrum from a deep GBT pointing toward J2000 =  $00^{\text{h}}15^{\text{m}} + 46^\circ 00'$ . The component at  $-238 \text{ km s}^{-1}$  has a velocity similar to M31's HVCs while the component at  $-388 \text{ km s}^{-1}$  is closer to the systemic velocity of M31. [b] Spectrum from a pointing toward J2000 =  $00^{\text{h}}20^{\text{m}} + 47^\circ 00'$ . The spectral line lies  $\sim 50 \text{ km s}^{-1}$  from Milky Way emission.

data. We detect no emission at  $\delta = +45^\circ$ , at only one position at  $\delta = +46^\circ$ , and yet have four detections at  $\delta = +47^\circ$ , two of which lie outside the lowest BT04 contour. The first conclusion must be that the HI is much patchier than would be inferred from BT04, which does not give a good representation of the HI at  $V_{\text{LSR}} \leq -150 \text{ km s}^{-1}$ . In this sense the M31 north measurements complement the conclusion from the M31-M33 field (Figure 4). In the GBT data, bright lines identified with Milky Way emission are regularly found at  $V_{\text{LSR}} \approx -100 \text{ km s}^{-1}$ . It is possible that the BT04 map includes some of this material, which might account for the discrepancy with the GBT measurements. Our detection of HI outside the BT04 contours at  $\delta = +47^\circ$  would imply that we are seeing very small angular sized features that suffer from beam dilution in the BT04 measurements. This was also a conclusion from Paper I.

The position at  $00^{\text{h}}15^{\text{m}} + 46^\circ 00'$  has two  $21\text{cm}$  line components separated by  $150 \text{ km s}^{-1}$ . Figure 9a shows this spectrum as well as the spectrum at  $00^{\text{h}}20^{\text{m}} + 47^\circ 00'$  (9b). Both illustrate the emission near  $-100 \text{ km s}^{-1}$  that we attribute to a component of the Milky Way.

#### 5. KINEMATICS OF THE EMISSION

Velocities of all GBT detections are shown in Figure 10 as the Local Group Standard of Rest velocity ( $V_{\text{LGRS}}$ ) versus angular distance from M31. We include both the clouds of Figure 2 and the detections to the north of M31. For comparison, the known HVCs around M31 and M33 are indicated with red circles (Westmeier et al. 2008; Grossi et al. 2008; Putman et al. 2009) and the systemic velocities of M31 and M33 with blue rectangles (Karachentsev & Makarov 1996). As discussed in Paper I, the clouds between M31 and M33 lie at velocities similar to the systemic velocity of both galaxies, and at a larger distance from either galaxy than their HVCs. This is true also of the two newly-identified clouds between M31 and M33. Most of the emission to the north of M31 appears consistent with arising in an extension of the M31 HVC population. It is in the velocity range associated by Lehner et al. (2015) with the circumgalactic medium of M31.

**Table 3**  
Observations North of M31

J2000 (hh:mm dd:mm) (1)	Galactic l°, b° (2)	$\sigma_T$ (mK) (3)	$T_L$ (mK) (4)	$V_{LSR}$ (km s <sup>-1</sup> ) (5)	FWHM (km s <sup>-1</sup> ) (6)	$N_{HI}$ (10 <sup>17</sup> cm <sup>-2</sup> ) (7)	$V_{LGSR}$ (km s <sup>-1</sup> ) (8)	$\rho$ (kpc) (9)
00:10 +46:00		3.8						
00:10 +47:00	115.6, -15.3	4.4	27.5 ± 1.3	-176 ± 1	25.9 ± 1.4	13.8 ± 1.0	106	115
00:15 +46:00	116.3, -16.4	3.5	15.6 ± 1.2	-238 ± 1	16.0 ± 1.4	4.8 ± 0.6	43	96
		3.5	22.4 ± 1.2	-388 ± 1	23.6 ± 1.4	10.2 ± 0.8	-109	
00:15 +47:00		3.3						
00:20 +45:00		6.4						
00:20 +47:00	117.4, -15.5	3.3	30.4 ± 1.0	-166 ± 1	26.1 ± 1.0	15.4 ± 0.7	112	98
00:20 +48:00		3.6						
00:25 +45:00		3.8						
00:25 +47:00		3.7						
00:30 +45:00		4.1						
00:30 +46:00		4.4						
00:30 +47:00		4.5						
00:35 +45:00		4.1						
00:35 +47:00		3.7						
00:40 +45:00		3.3						
00:40 +46:00		3.8						
00:40 +47:00	120.9, -15.8	2.9	18.3 ± 0.7	-182 ± 1	25.1 ± 1.1	8.9 ± 0.6	85	81
00:45 +47:00	121.8, -15.9	3.7	18.8 ± 0.8	-183 ± 1	42.5 ± 2.1	15.5 ± 1.0	86	80

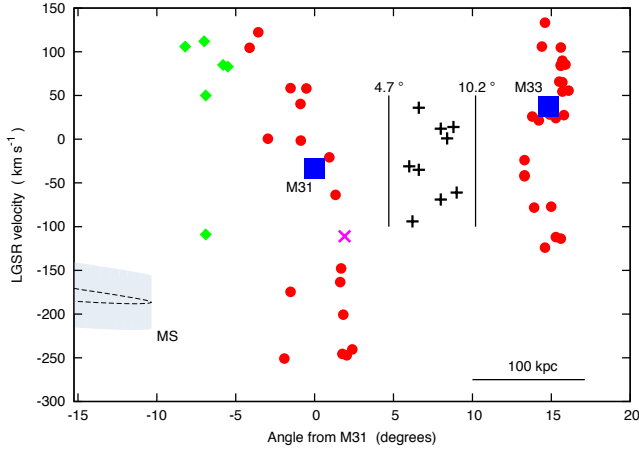


**Figure 10.** Velocity with respect to the Local Group Standard of Rest ( $V_{LGSR}$ ) versus angular distance from M31, where directions toward M33 are taken to be positive. The blue squares are M31 and M33, with the red dots being the high velocity cloud populations of each galaxy. The black crosses are the clouds from the M31-M33 map with vertical lines marking the map limits. The green diamonds are detections from the GBT pointings north of M31. The pink cross marks the UV absorption line measurements of Koch et al. (2015) towards a background AGN. The MS curve is the estimated position of Stream S0 from Nidever et al. (2010), with  $\pm 30$  km s<sup>-1</sup> spread to account for the velocity width of the Stream and our approximations. In most cases the Stream lies hundreds of km s<sup>-1</sup> away from the emission we detect. The rotation of M31 extends from -353 to +248 km s<sup>-1</sup> in  $V_{LGSR}$ , and for M33 from -105 to +158 km s<sup>-1</sup> (Braun et al. 2009; Putman et al. 2009).

Koch et al. (2015) report detection of gas possibly associated with the M31 Stellar Stream through UV absorption line measurements against background AGN. Their most secure detection is in lines of Si, C, and O against Q0045+3926 at a location about 2° from M31 in the direction of M33. They find one system at  $V_{LSR} = -370$  km s<sup>-1</sup>, or  $V_{LGSR} = -111$  km s<sup>-1</sup>, which is marked with a pink cross in Figure 10. It lies in the region occupied by M31 HVCs.

The second HI component toward 00<sup>h</sup>15<sup>m</sup>, +46°00' (Figure 9a) at  $V_{LSR} = -388$  km s<sup>-1</sup> ( $V_{LGSR} = -109$

km s<sup>-1</sup>) has a velocity that might be associated with the Magellanic Stream (Lehner et al. 2015) though this direction lies nearly 20° from the axis of the Magellanic Stream as defined by Nidever et al. (2010), and not far from a direction that does not show UV absorption arising in the Stream (Fox et al. 2014). As our measurements are only over a sparse grid in this area, we do not know the size or mass of any cloud associated with this feature. One of the M31 HVCs, the Davies Cloud, has also been suspected of being part of the Stream because its mass would be an order of magnitude larger than the other M31 HVCs were it at the distance of M31 (Davies 1975; Westmeier et al. 2008). The Davies Cloud does not have extraordinary kinematics and does not occupy an unusual location in Figure 10. At the distance of M31 its HI mass is similar to that of the Milky Way HVC Complex C (Wakker et al. 2007a). We see no reason to exclude it from the M31 HVC population.

Because Nidever et al. (2010) have shown that the Magellanic Stream (MS) extends into the BT04 area, we have tried to estimate where the MS would lie in Figure 10. Five HI Streams were identified in the BT04 data from Nidever et al. (2010, Figure 4), labeled S0-S4. We take Stream S0, the one closest to our pointings, to lie along a line of constant RA at 23<sup>h</sup>45<sup>m</sup> and choose a declination range from +20 to +50 degrees.

To approximate the LGSr velocities of Stream S0 along this line, we first transform the positions to Magellanic Longitude ( $L_{MS}$ , Nidever et al. 2008) and use the extended  $V_{LSR}$  vs.  $L_{MS}$  fiducial curve from Figure 7b of Nidever et al. (2010), converting to  $V_{LGSR}$ . The resulting angle-velocity for Stream S0 is shown as a dashed curve in Figure 10. To account for the spread in velocity of the Stream, and for our approximations, we over-plot a shaded region with bounds of  $\pm 30$  km s<sup>-1</sup> from the curve.

The point of closest approach of S0 to M31 is at an angular distance of 10.3° with  $V_{LGSR} = -187$  km s<sup>-1</sup>. Most of our detections to the northwest of M31 lie at least 225 km s<sup>-1</sup> from the average velocity of S0 ( $V_{LGSR} \approx -175$



km s<sup>-1</sup>). The line at 00<sup>h</sup>15<sup>m</sup> + 46°00',  $V_{\text{LSR}} = -109$  km s<sup>-1</sup> is the only one within 5° and 50 km s<sup>-1</sup> of S0, so excepting this, it seems unlikely that the emission we detect arises in the Magellanic Stream.

## 6. DISCUSSION: THE ORIGIN OF THE CLOUDS BETWEEN M31 AND M33

In the 12 square-degree area between M31 and M33 observed with the GBT, the faint HI discovered by BT04 is resolved into at least nine discrete clouds. Here we consider possibilities for the origin of the clouds.

### 6.1. Products of Galaxy Interactions

Although BT04 surveyed a large area, they found HI at relevant velocities only near a line joining M31 and M33 on the sky (Figure 1), and not widespread in the Local Group. This naturally leads to models where the HI tracks past tidal interactions, as in the M81 group (Yun et al. 1994; Chynoweth et al. 2008). Bekki (2008) modeled the BT04 results as arising from a close encounter between M31 and M33 some 4-8 Gyr ago, and others have also considered an interaction a few Gyr ago as an explanation for features in M33's extended HI distribution and the stellar structures in M31 and M33 (Putman et al. 2009; McConnachie et al. 2009; Lewis et al. 2013). The Magellanic Stream is a good, nearby template of an ongoing galaxy interaction (e.g., Besla et al. 2010; Stanimirovic et al. 2010) but its age is quite uncertain, in the range of 0.3 - 2.0 Gyr (D'Onghia & Fox 2015). The HI mass and average  $N_{\text{HI}}$  is generally higher than we observe between M31 and M33 (Stanimirović et al. 2008; Nidever et al. 2008, 2010). It is worth noting that as gaseous tidal debris ages it should disperse causing its  $N_{\text{HI}}$  to decrease, so the M31-M33 clouds may represent material that is substantially older than is seen in the Magellanic Stream.

A recent study of the evolution of the Local Group has now cast doubt on the possibility that we are observing the relic of a past interaction between M31 and M33, as it indicates that in the last  $\approx 12$  Gyr, M33 has not been closer to M31 than it is now (Shaya & Tully 2013). The same calculations though, suggest that the dwarf galaxies And II and And XV could have interacted with M31 over the last 0.7 Gyr creating an HI extension toward M33. Since Local Group dwarfs with detectable HI typically have  $M_{\text{HI}}/L_V \sim 1$  (McConnachie 2012; Spekkens et al. 2014), we can estimate how much HI And II and And XV could have contributed to the M31 CGM. Based on the  $M_V$  from McConnachie (2012), their total HI mass would be  $\sim 10^7 M_\odot$ , which is comparable to the total HI mass in the entire filamentary structure between M31 and M33. It seems unlikely, however, that the encounter would leave the nine clouds we detect, each apparently coherent, but spread over a projected distance of 70 kpc with a spread in  $V_{\text{LSR}}$  of 130 km s<sup>-1</sup>. It is clear that more detailed modelling of the Local Group, including its gas, is needed to address these possibilities.

### 6.2. Dwarf Galaxies

The larger M31-M33 clouds have an HI mass similar to that of some dwarf galaxies, but the clouds are not likely to be associated with stellar systems. Table 4 compares properties of the most massive cloud with dwarf galaxies

of a similar HI mass. The dwarf spheroidal And XII is included as it is one of the faintest of the known M31 satellites, but was detected easily in a recent search for even fainter systems (Martin et al. 2013). To allow for accurate comparisons we calculate dynamical masses from the measured quantities in Table 4, using Eq. 2.

Local Group dwarfs with detectable HI typically have a stellar mass similar to their gas mass (Spekkens et al. 2014). For Cloud 6 this would imply  $M_V < -8$ , and its stars would certainly have been detected already. Martin et al. (2013) report a possible stellar feature at the Cloud 6 position, but is considerably fainter than And XII, and if it is actually associated with the Cloud, would imply  $M_{\text{HI}}/M_* > 10$ . The dynamical mass of Cloud 6 is also about an order of magnitude higher than that of Leo P, even though Leo P has  $\sim 10$  times more baryonic mass. Using the relationship between total mass and  $M_V$  from the Local Group data of McConnachie (2012), Cloud 6 – indeed most of the clouds detected in HI between M31 and M33 – should have a stellar counterpart with  $M_V < -13$ , whereas the surveys of stars near M31 suggest  $M_V > -6$ . If Cloud 6 is a galaxy it is one with rather extreme properties. It will be interesting to see if the possible association with a slight stellar overdensity discovered by Martin et al. (2013) reveals a real stellar component of this cloud. The dwarf galaxy Leo P has a small rotational velocity,  $15 \pm 5$  km s<sup>-1</sup>, comparable to its velocity dispersion (Bernstein-Cooper et al. 2014). As shown in Figure 7, Cloud 6 shows a slight gradient in  $V_{\text{LSR}}$  from center to edge; at our angular resolution any rotational component is comparable to or smaller than its velocity dispersion.

Another reason why the M31-M33 clouds are not likely to be galaxies is that the stellar satellites of M31 and the Milky Way that lie closer than  $\approx 300$  kpc to the parent galaxy are extremely deficient in HI, with mass limits typically well below  $10^4 M_\odot$ . In some cases  $M_{\text{HI}} \leq 100 M_\odot$  (Grcevich & Putman 2009; Spekkens et al. 2014, R. Beaton private communication). The two M31 satellite galaxies that lie nearest the M31-M33 field, And II with  $V_{\text{LSR}} = -187$  km s<sup>-1</sup>, and And XV with  $V_{\text{LSR}} = -322$  km s<sup>-1</sup>, are among those that lack detectable HI emission (Lockman et al. 2012). Apparently M31 and the Milky Way are very efficient at stripping gas from small satellites passing through their CGM (Mayer et al. 2006; Grcevich & Putman 2009; Nickerson et al. 2011; Gatto et al. 2013).

Figure 11 contains the same HI data as Figure 10 but instead of the M31 and M33 HVCs, the location and velocity of dwarf galaxies from McConnachie (2012) are shown. There is no obvious connection between the dwarf galaxies and the HI clouds as the dwarfs are spread over 400 km s<sup>-1</sup> while the clouds have an average  $V_{\text{LSR}}$  like that of M31 and M33 and a total range of only 130 km s<sup>-1</sup>.

### 6.3. High Velocity Clouds and Dark Matter Sub-Halos

Table 5 gives information that allows us to compare the M31-M33 clouds with various populations of HVCs. For the M31-M33 clouds, values are the median from Table 2. For the M31 HVCs the listed radius is the median found by Westmeier et al. (2005) while the FWHM and  $M_{\text{HI}}$  are the median values from Westmeier et al. (2008). Values for the Ultra-Compact HVCs (UCHVC) are from

**Table 4**  
Comparison of an M31-M33 Cloud with Dwarf Galaxies

Object	$r_{1/2}$ (kpc)	FWHM <sup>b</sup> ( $\text{km s}^{-1}$ )	$M_{\text{HI}}$ ( $M_{\odot}$ )	$M_*$ ( $M_{\odot}$ )	$M_V$ (mag)	$M_{\text{dyn}}$ ( $M_{\odot}$ )	References
(1)	(2)	(3)	(4)	(5)	(6)	(7)	(8)
Cloud 6 <sup>a</sup>	0.78	34	$3.9 \times 10^5$	—	—	$2.2 \times 10^8$	a
Leo P	0.25	24	$9.5 \times 10^5$	$5.7 \times 10^5$	-9.4	$3.6 \times 10^7$	b,c,d
Leo T	0.17	16	$2.8 \times 10^5$	$1.4 \times 10^5$	-8.0	$1.1 \times 10^7$	e,f,g,h
And XII	0.30	6	—	$3.1 \times 10^4$	-6.4	$2.8 \times 10^6$	i,j

**References.** — (a) This Work; (b) Bernstein-Cooper et al. (2014); (c) Adams et al. (2013); (d) McQuinn et al. (2013); (e) Ryan-Weber et al. (2008); (f) Simon & Geha (2007); (g) Faerman et al. (2013); (h) de Jong et al. (2008); (i) Collins et al. (2010); (j) McConnachie (2012)

<sup>a</sup> For an assumed distance of 800 kpc.

<sup>b</sup> Of the HI emission except for And XII where it is from the stars.

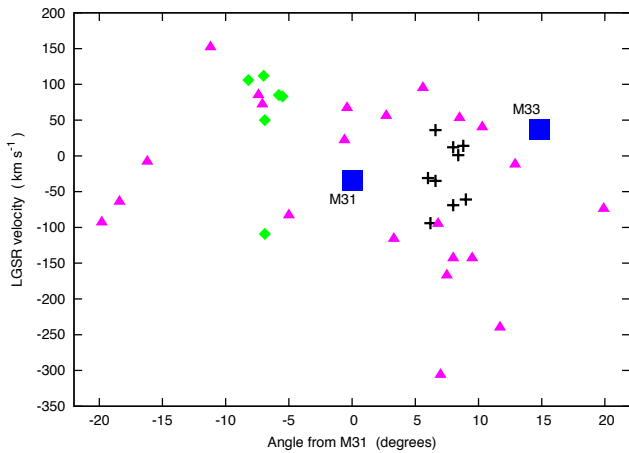


**Figure 11.** Velocity with respect to the Local Group Standard of Rest ( $V_{\text{LSGR}}$ ) versus angular distance from M31, where directions toward M33 are taken to be positive. The blue squares are M31 and M33, and the black crosses are the clouds from the M31-M33 map. The green diamonds are detections from the GBT pointings north of M31. The pink triangles are dwarf galaxies from the compilation of McConnachie (2012). There is no apparent connection between the dwarf galaxies and the M31-M33 HI clouds.

Adams et al. (2013) scaled to a distance of 800 kpc.

There is considerable overlap between the physical properties of the M31-M33 clouds and the M31 HVCs, but much less so between their locations and kinematics. Many HVCs are located close to the edge of the M31 disk in intersecting filaments (Westmeier et al. 2005). Although median line widths are similar, the M31 HVCs have widths as low as half and as high as twice the FWHM of the M31-M33 clouds; 90% have a FWHM in the range  $13\text{--}67 \text{ km s}^{-1}$ , whereas the entire sample of M31-M33 clouds has FWHMs between 19 and  $39 \text{ km s}^{-1}$ . The HVCs also have a median mass four times larger than the clouds. Indeed, there is no cloud in our sample that has an HI mass as high as the median HI mass of the M31 HVCs. Most importantly, the kinematics of the clouds differ significantly from that of the HVCs near them (Figure 10), and they have a substantially smaller spread in velocity (see also Paper I). With only one exception the detections north of M31 have positions and velocities consistent with being part of the M31 HVC population while the nine clouds between M31 and M33 do not. The M31 HVCs in the direction of M33 have considerably more negative velocities than the systemic

velocity of M31. For M31  $V_{\text{LSGR}} = -34 \text{ km s}^{-1}$ , while its HVCs towards M33 have  $\langle V_{\text{LSGR}} \rangle = -166 \text{ km s}^{-1}$ . In contrast, the M31-M33 clouds have  $\langle V_{\text{LSGR}} \rangle = -25 \text{ km s}^{-1}$ . The clouds do not appear to be simply an extension of the M31 HVC population. Still, the physical properties displayed in Table 5 suggest that the two populations may be formed by similar processes, and that the UCHVCs, if at a similar distance, have similar properties as well.

Thilker et al. (2004) and Westmeier et al. (2005) considered whether the HVCs of M31 might be the baryonic component of a population of low-mass dark matter halos, an idea with a long history in the study of HVCs (Oort 1966; Blitz et al. 1999; Braun & Burton 1999; de Heij et al. 2002; Nichols et al. 2014). Of particular importance is that some HVCs (and some dwarf galaxies) show a two-component structure in their 21cm lines, suggesting the presence of gas in equilibrium at two temperatures. This is a diagnostic of pressure, and was used (among other pieces of evidence) to argue that the compact HVCs (CHVCs) must lie at distances  $\lesssim 150 \text{ kpc}$  from the Milky Way, and not at distances of  $\sim 1 \text{ Mpc}$  (Sternberg et al. 2002). The failure to detect CHVC analogs spread throughout other groups of galaxies also implies that they must be located within 90 kpc of individual galaxies (Pisano et al. 2007). This result is consistent with HVC detections around other galaxies such as NGC 891 and NGC 2403 (Oosterloo et al. 2007; Fraternali et al. 2002) and the distance brackets for Milky Way HVCs (e.g. Wakker 2001; Wakker et al. 2007b, 2008).

The UCHVCs are discussed in depth in Adams et al. (2013) and Faerman et al. (2013). The dwarf galaxy Leo P was originally classified as a UCHVC on the basis of its 21cm characteristics before its stellar component was detected and it was discovered to be at a distance of 1.7 Mpc (Giovanelli et al. 2013; Rhode et al. 2013; McQuinn et al. 2013). The HI properties listed in Table 5 for the UCHVCs show that they are similar to the M31 HVCs and the M31-M33 clouds. There is no evidence for a two-phase interstellar medium in the M31 HVCs, the M31-M33 clouds, or in the unidentified UCHVCs, although it is found in other HVCs and the Magellanic Stream (Kalberla & Haud 2006; Stanimirovic et al. 2010). This is important as it implies that these objects exist in regions of low external pressure (Sternberg et al. 2002). The observations to date, however, have relatively poor

**Table 5**  
Comparison M31-M33 Clouds with HVCs

Object	$r_{1/2}$ (kpc)	FWHM (km s <sup>-1</sup> )	$M_{\text{HI}}$ ( $M_{\odot}$ )	$M_{\text{dyn}}$ ( $M_{\odot}$ )	References
(1)	(2)	(3)	(4)	(5)	(6)
M31-M33 Clouds	0.75	27	$1.2 \times 10^5$	$1.4 \times 10^8$	a
M31 HVC	0.52	26	$4.7 \times 10^5$	$8.8 \times 10^7$	b, c
UCHVC	1.16	23	$1.2 \times 10^5$	$1.5 \times 10^8$	d

**References.** — (a) This Work; (b) Westmeier et al. (2005); (c) Westmeier et al. (2008); (d) Adams et al. (2013)

linear resolution and might not be able to detect a cool HI phase if present in moderate amounts.

#### 6.4. Gas in Planes of Satellites or a Dark Matter Filament

Lacking an estimate of the distance to the clouds, it is not clear if they are related to the planes of satellite galaxies that are now thought to be fundamental structures in the Local Group (Ibata et al. 2013; Conn et al. 2012, 2013). The M31-M33 field studied here lies in the part of the sky where M31 satellites are aligned in the structure called “Plane 2”. It lies to the west of M31 and extends southwards towards M33 (Shaya & Tully 2013). The two M31 satellite galaxies nearest to our field on the sky have velocities within the range of the HI clouds (see Figure 3 of Shaya & Tully (2013)) and it is an intriguing possibility that the M31-M33 clouds are part of a larger alignment of matter in this part of the Local Group. Although study of these planes is only beginning, if they represent large-scale dark matter structures, then it is very plausible that they would be accompanied by enhancements in gas density.

BT04 suggested that the HI they discovered originated from condensation of hot gas in a dark matter filament connecting M31 and M33. This is now testable, in part, through cosmological simulations that attempt to follow the evolution of systems like the Local Group. Nuza et al. (2014) and Scannapieco et al. (2015) have analyzed the simulation of a group containing two galaxies like M31 and the Milky Way, and while M33 is considerably less massive than the Milky Way, the simulation might still have some application to the M31-M33 region. They find that the hot gaseous halos of the M31 and Milky Way analogs overlap and that they evolve to occupy the same filament, leading to an excess of neutral gas between them that forms around  $z \sim 1$  and persists to the present. Clouds like those observed here might then condense in the filament. The current simulations do not have the resolution to detect anything as small as the M31-M33 clouds, and it is not clear that M31 and M33 would have similar overlapping gas halos, but these results are encouraging that intra-group gas might be a natural feature of systems like the Local Group.

In view of the evidence that M31 has a massive CGM, as discussed in the next section, it will be important to determine if the direction of M33 is enhanced in total material, as would be suggested by this scenario.

#### 6.5. Condensations in the M31 Circumgalactic Medium

While the presence of the clouds between M31 and M33 is unexpected, the total mass involved is not large com-

pared to the baryonic mass at that location in the halo of M31 as determined from recent measurements. The observed  $N_{\text{HI}}$  averaged over our field is only  $9 \times 10^{16} \text{ cm}^{-2}$ . Lehner et al. (2015) have studied the extended CGM of M31 through measurement of UV absorption lines against background QSOs out to a projected distance  $> 500$  kpc, an area that covers not only the M31-M33 clouds, but the galaxy M33 as well. They find that the total gas mass in the M31 CGM may be  $> 10^{10} M_{\odot}$  with an ionization fraction  $> 90\%$ . The Lehner et al. radial column density profile of SiII evaluated at the projected distance  $\rho \approx 100$  kpc of the M31-M33 field predicts  $N_{\text{SiII}} = 2.1 \times 10^{13} \text{ cm}^{-2}$ , which implies an average total column density  $N_{\text{H}} = 6 \times 10^{17} (Z_{\odot}/Z) \text{ cm}^{-2}$ . Thus, if the CGM of M31 has a sub-solar metallicity, even if it is  $> 90\%$  ionized, it would have a neutral component of similar magnitude to the average  $N_{\text{HI}}$  of the clouds over our field.

The tight kinematic pattern of the M31-M33 clouds suggests that they are not spread along the several hundred kpc path through the M31 halo, so arguments about their origin in the M31 CGM are suggestive at best. The Lehner et al. (2015) measurements, however, allow the possibility that the existence of clouds at  $\rho = 100$  kpc from M31 does not require a major enhancement to the mass or density of its CGM, but could result from a restructuring or phase change in material already present, triggered, perhaps by the passage of a satellite as suggested by Shaya & Tully (2013), or by a concentration of mass in a plane of satellites.

The so called “galactic fountain” model of gas accretion (e.g. Bregman 1980; Shapiro & Field 1976) states that supernovae kick material above the disk of a spiral galaxy, which then rains back down onto the disk as it cools. More recent work has shown that this fountain material can cause the surrounding halo material to condense and fall onto the disk as well (Fraternali & Binney 2008; Fraternali et al. 2015). While the M31-M33 clouds are too far away from either galaxy to be triggered by a galactic fountain, it is possible that hot gas could be triggered to condense by other external sources, such as the motion of a satellite galaxy through the CGM. Such a satellite galaxy would presumably need to contain at least some cold gas to serve as a trigger. It would be interesting to evaluate this mechanism in the context of the M31 CGM.

## 7. SUMMARY

Prompted by the discovery of extended regions of very faint HI that appear to form a partial bridge connecting M31 and M33 (Braun & Thilker 2004), we have measured

21cm HI emission in a 12 square-degree region between M31 and M33 with the Green Bank Telescope at 9'1 angular resolution reaching  $5\sigma$  limits on  $N_{\text{HI}}$  of  $3.9 \times 10^{17} \text{ cm}^{-2}$  for a  $30 \text{ km s}^{-1}$  line. Sensitive observations were also made at 18 locations on a grid to the north of M31.

The new data confirm and extend the basic picture derived from the preliminary data presented in Paper I: in this region between M31 and M33 the HI is largely if not entirely contained in discrete neutral clouds that each have  $M_{\text{HI}}$  reaching a few  $10^5 M_{\odot}$ , lying at a projected distance  $\approx 100 \text{ kpc}$  from M31. We do not find any evidence for a more diffuse component of HI, and attribute our claim for this in Paper I to systematic instrumental baseline effects at the level of a few mK. We measure only 63% of the HI mass found by BT04 in this region. While we present a possible explanation for this discrepancy (§3.2), its origin is uncertain. The clouds appear to be spatially and kinematically independent from each other and can have velocities that differ by  $> 100 \text{ km s}^{-1}$  over projected distances  $\sim 10 \text{ kpc}$ . Our HI mass limits of  $\sim 10^4 M_{\odot}$  are lower, by an order of magnitude or more, than other surveys of galaxy groups (e.g. Auld et al. 2006; Chynoweth et al. 2008). Thus these objects may represent a new, previously undetected population.

The clouds have a dynamical mass nearly a thousand times their HI mass and strong limits on any stellar component, making it unlikely that they are part of the dwarf galaxy system of the Local Group. Indeed, dwarf galaxies near large spirals in the Local Group completely lack detectable HI (Grcevich & Putman 2009; Spekkens et al. 2014; Westmeier et al. 2015, R. Beaton private communication). The clouds have kinematics more similar to the systematic velocity of the galaxies than to the HVC system of M31 and M33, but the clouds have HI properties like those of the M31 HVCs and the class of ultra-compact HVCs (Westmeier et al. 2005, 2008; Adams et al. 2013).

Numerical simulations of the evolution of the Local Group produce regions of neutral gas between the major galaxies that may be analogs to the detected clouds (Nuza et al. 2014) though considerably larger and more massive. If M31 has the very extensive circumgalactic medium (CGM) recently proposed by Lehner et al. (2015), then it contains  $\sim 10$  times the column density of gas needed for formation of the clouds at their projected radius. The clouds might then be condensations in the 90% ionized M31 CGM marking a past interaction with one or more of the dwarf galaxies (Shaya & Tully 2013). It will be critical in understanding the clouds to have an accurate census of the CGM of M31 to determine if the M31-M33 direction is indeed a region of enhanced total mass.

Our results to the north-west of M31 are still too incomplete to determine if we have detected anything like the population of clouds that exist between M31 and M33, but the data do suggest that the HVC population of M31 extends to  $\rho \approx 100 \text{ kpc}$  in the north-west, much further than previously known. A similar extension to the south-east is not observed. The detection of HI outside the BT04 contours at  $\delta = +47^\circ$  would imply that we are seeing very small angular sized features that are beam-diluted in the BT04 measurements. Complete mapping of this area with the GBT is underway to resolve the discrepancy.

We thank Rachel Beaton for sharing results of her GBT survey of M31 dwarf galaxies before publication. S.A.W. acknowledges partial support from the student observing support grant (GSSP11-012) provided by the NRAO. D.J.P. and S.A.W. acknowledge partial support from NSF CAREER grant AST-1149491.

## REFERENCES

- Adams, E. A. K., Giovanelli, R., & Haynes, M. P. 2013, *ApJ*, 768, 77
- Auld, R., Minchin, R. F., Davies, J. I., et al. 2006, *MNRAS*, 371, 1617
- Bekki, K. 2008, *MNRAS*, 390, L24
- Bernstein-Cooper, E. Z., Cannon, J. M., Elson, E. C., et al. 2014, *AJ*, 148, 35
- Besla, G., Kallivayalil, N., Hernquist, L., et al. 2010, *ApJL*, 721, L97
- Binney, J., & Tremaine, S. 2008, *Galactic Dynamics: Second Edition* (Princeton University Press)
- Blitz, L., Spergel, D. N., Teuben, P. J., Hartmann, D., & Burton, W. B. 1999, *ApJ*, 514, 818
- Bono, G., Caputo, F., Marconi, M., & Musella, I. 2010, *ApJ*, 715, 277
- Boothroyd, A. I., Blagrove, K., Lockman, F. J., et al. 2011, *A&A*, 536, A81
- Braun, R., & Burton, W. B. 1999, *A&A*, 341, 437
- Braun, R., & Thilker, D. A. 2004, *A&A*, 417, 421
- Braun, R., Thilker, D. A., Walterbos, R. A. M., & Corbelli, E. 2009, *ApJ*, 695, 937
- Bregman, J. N. 1980, *ApJ*, 236, 577
- Cen, R. 2013, *ApJ*, 770, 139
- Chen, H.-W., Helsby, J. E., Gauthier, J.-R., et al. 2010, *ApJ*, 714, 1521
- Chynoweth, K. M., Langston, G. I., Yun, M. S., et al. 2008, *AJ*, 135, 1983
- Collins, M. L. M., Chapman, S. C., Irwin, M. J., et al. 2010, *MNRAS*, 407, 2411
- Conn, A. R., Ibata, R. A., Lewis, G. F., et al. 2012, *ApJ*, 758, 11
- Conn, A. R., Lewis, G. F., Ibata, R. A., et al. 2013, *ApJ*, 766, 120
- Davé, R., Cen, R., Ostriker, J. P., et al. 2001, *ApJ*, 552, 473
- Davies, R. D. 1975, *MNRAS*, 170, 45P
- de Heij, V., Braun, R., & Burton, W. B. 2002, *A&A*, 392, 417
- de Jong, J. T. A., Harris, J., Coleman, M. G., et al. 2008, *ApJ*, 680, 1112
- D'Onghia, E., & Fox, A. J. 2015, *ArXiv e-prints*
- Faerman, Y., Sternberg, A., & McKee, C. F. 2013, *ApJ*, 777, 119
- Fox, A. J., Wakker, B. P., Barger, K. A., et al. 2014, *ApJ*, 787, 147
- Fraternali, F., & Binney, J. J. 2008, *MNRAS*, 386, 935
- Fraternali, F., Marasco, A., Armillotta, L., & Marinacci, F. 2015, *MNRAS*, 447, L70
- Fraternali, F., van Moorsel, G., Sancisi, R., & Oosterloo, T. 2002, *AJ*, 123, 3124
- Fukugita, M., & Peebles, P. J. E. 2006, *ApJ*, 639, 590
- Gatto, A., Fraternali, F., Read, J. I., et al. 2013, *MNRAS*, 433, 2749
- Giovanelli, R., Haynes, M. P., Adams, E. A. K., et al. 2013, *AJ*, 146, 15
- Grcevich, J., & Putman, M. E. 2009, *ApJ*, 696, 385
- Grossi, M., Giovanardi, C., Corbelli, E., et al. 2008, *A&A*, 487, 161
- Heald, G., Józsa, G., Serra, P., et al. 2011, *A&A*, 526, A118
- Ibata, R. A., Lewis, G. F., Conn, A. R., et al. 2013, *Nature*, 493, 62
- Kalberla, P. M. W., & Haud, U. 2006, *A&A*, 455, 481
- Karachentsev, I. D., & Makarov, D. A. 1996, *AJ*, 111, 794
- Koch, A., Danforth, C. W., Rich, R. M., Ibata, R., & Keeney, B. A. 2015, *ArXiv e-prints*
- Lehner, N., Howk, J. C., Thom, C., et al. 2012, *MNRAS*, 424, 2896
- Lehner, N., Howk, J. C., & Wakker, B. P. 2015, *ApJ*, 804, 79
- Lewis, G. F., Braun, R., McConnachie, A. W., et al. 2013, *ApJ*, 763, 4
- Lockman, F. J., Free, N. L., & Shields, J. C. 2012, *AJ*, 144, 52

- Mangum, J. G., Emerson, D. T., & Greisen, E. W. 2007, *A&A*, 474, 679
- Marganian, P., Garwood, R. W., Braatz, J. A., Radziwill, N. M., & Maddalena, R. J. 2006, in *Astronomical Society of the Pacific Conference Series*, Vol. 351, *Astronomical Data Analysis Software and Systems XV*, ed. C. Gabriel, C. Arviset, D. Ponz, & S. Enrique, 512
- Martin, N. F., Ibata, R. A., McConnachie, A. W., et al. 2013, *ApJ*, 776, 80
- Mayer, L., Mastropietro, C., Wadsley, J., Stadel, J., & Moore, B. 2006, *MNRAS*, 369, 1021
- McConnachie, A. W. 2012, *AJ*, 144, 4
- McConnachie, A. W., Irwin, M. J., Ibata, R. A., et al. 2009, *Nature*, 461, 66
- McQuinn, K. B. W., Skillman, E. D., Berg, D., et al. 2013, *AJ*, 146, 145
- Nichols, M., Mirabal, N., Agertz, O., Lockman, F. J., & Bland-Hawthorn, J. 2014, *MNRAS*, 442, 2883
- Nickerson, S., Stinson, G., Couchman, H. M. P., Bailin, J., & Wadsley, J. 2011, *MNRAS*, 415, 257
- Nidever, D. L., Majewski, S. R., & Burton, W. B. 2008, *ApJ*, 679, 432
- Nidever, D. L., Majewski, S. R., Butler Burton, W., & Nigra, L. 2010, *ApJ*, 723, 1618
- Nuza, S. E., Parisi, F., Scannapieco, C., et al. 2014, *MNRAS*, 441, 2593
- Oort, J. H. 1966, *Bull. Astron. Inst. Netherlands*, 18, 421
- Oosterloo, T., Fraternali, F., & Sancisi, R. 2007, *AJ*, 134, 1019
- Pisano, D. J., Barnes, D. G., Gibson, B. K., et al. 2007, *ApJ*, 662, 959
- Popping, A., & Braun, R. 2008, *A&A*, 479, 903
- Prestage, R. M., Constantikes, K. T., Hunter, T. R., et al. 2009, *IEEE Proceedings*, 97, 1382
- Putman, M. E., Peek, J. E. G., & Jounge, M. R. 2012, *ARA&A*, 50, 491
- Putman, M. E., Peek, J. E. G., Muratov, A., et al. 2009, *ApJ*, 703, 1486
- Rhode, K. L., Salzer, J. J., Haurberg, N. C., et al. 2013, *AJ*, 145, 149
- Riess, A. G., Fliri, J., & Valls-Gabaud, D. 2012, *ApJ*, 745, 156
- Ryan-Weber, E. V., Begum, A., Oosterloo, T., et al. 2008, *MNRAS*, 384, 535
- Scannapieco, C., Creasey, P., Nuza, S. E., et al. 2015, *A&A*, 577, A3
- Sembach, K. R., Wakker, B. P., Savage, B. D., et al. 2003, *ApJS*, 146, 165
- Shapiro, P. R., & Field, G. B. 1976, *ApJ*, 205, 762
- Shaya, E. J., & Tully, R. B. 2013, *MNRAS*, 436, 2096
- Shull, J. M., Jones, J. R., Danforth, C. W., & Collins, J. A. 2009, *ApJ*, 699, 754
- Simon, J. D., & Geha, M. 2007, *ApJ*, 670, 313
- Spekkens, K., Urbancic, N., Mason, B. S., Willman, B., & Aguirre, J. E. 2014, *ApJL*, 795, L5
- Stanimirovic, S., Gallagher, III, J. S., & Nigra, L. 2010, *Serbian Astronomical Journal*, 180, 1
- Stanimirović, S., Hoffman, S., Heiles, C., et al. 2008, *ApJ*, 680, 276
- Sternberg, A., McKee, C. F., & Wolfire, M. G. 2002, *ApJS*, 143, 419
- Thilker, D. A., Braun, R., Walterbos, R. A. M., et al. 2004, *ApJL*, 601, L39
- Wakker, B. P. 2001, *ApJS*, 136, 463
- Wakker, B. P., York, D. G., Wilhelm, R., et al. 2008, *ApJ*, 672, 298
- Wakker, B. P., York, D. G., Howk, J. C., et al. 2007a, *ApJL*, 670, L113
- . 2007b, *ApJL*, 670, L113
- Westmeier, T., Brüns, C., & Kerp, J. 2005, *A&A*, 432, 937
- . 2008, *MNRAS*, 390, 1691
- Westmeier, T., Staveley-Smith, L., Calabretta, M., et al. 2015, *MNRAS*, 453, 338
- Wolfe, S. A., Pisano, D. J., Lockman, F. J., McGaugh, S. S., & Shaya, E. J. 2013, *Nature*, 497, 224
- Yun, M. S., Ho, P. T. P., & Lo, K. Y. 1994, *Nature*, 372, 530
- Zwaan, M. A. 2001, *MNRAS*, 325, 1142